Scientia Pharmaceutica

ÖSTERREICHISCHE PHARMAZEUTISCHE GESELLSCHAFT

MDPI

Article

Identifying and Evaluating Flavonoids as Potential Inhibitors of SARS-CoV-2 Main Protease (Mpro/3CL) Through Docking and Molecular Dynamics

Getulio Flores-Tlalpa [1,2], Lenin Domínguez-Ramírez [3], Luis Márquez-Domínguez [1], Julio Reyes-Leyva [4], Paulina Cortés-Hernández [5], Fabiola Domínguez [6], Jesús Hernández [7], Irma Herrera-Camacho [4] and Gerardo Santos-López [1,*]

1 Laboratorio de Virología, Centro de Investigación Biomédica de Oriente, Instituto Mexicano del Seguro Social, Atlixco 74360, Puebla, Mexico; amocualli-g-g@hotmail.com (G.F.-T.); lumardo80@gmail.com (L.M.-D.)
2 Posgrado en Ciencias Químicas, Benemérita Universidad Autónoma de Puebla, Puebla 72570, Mexico
3 Computational Biochemistry Laboratory, Centro de Investigación Biomédica de Oriente, Instituto Mexicano del Seguro Social (IMSS), Atlixco 74360, Puebla, Mexico; lenin.dominguez.ramierz@gmail.com
4 Centro de Química, Instituto de Ciencias, Benemérita Universidad Autónoma de Puebla, Puebla 72570, Mexico; jreyesleyva@gmail.com (J.R.-L.); irma.herrera@correo.buap.mx (I.H.-C.)
5 Laboratorio de Metadinámica y Salud de Poblaciones, Centro de Investigación Biomédica de Oriente, Instituto Mexicano del Seguro Social, Atlixco 74360, Puebla, Mexico; paulina.cortes.hernandez@gmail.com
6 Laboratorio de Biotecnología de Productos Naturales, Centro de Investigación Biomédica de Oriente, Instituto Mexicano del Seguro Social, Atlixco 74360, Puebla, Mexico; irmafabiola@yahoo.com
7 Laboratorio de Inmunología, Centro de Investigación en Alimentación y Desarrollo, A.C, Hermosillo 83304, Sonora, Mexico; jhdez@ciad.mx
* Correspondence: gerardo.santos.lopez@gmail.com

Abstract

Although the acute phase of the SARS-CoV-2 pandemic has subsided, the continued emergence of viral variants underscores the need for structurally diverse antiviral inhibitors. In this study, molecular docking followed by molecular dynamics (300 ns) simulations and binding free energy calculations using the Molecular Mechanics Poisson–Boltzmann Surface Area (MM-PBSA) method were employed to evaluate substituted flavonoids derived from *Taraxacum officinale* and *Urtica dioica* as potential inhibitors of the SARS-CoV-2 main protease (Mpro/3CLpro). Docking analysis identified several derivatives with favorable binding scores; however, dynamic refinement revealed differential stability among the ligand–protein complexes. Among the evaluated compounds, the luteolin derivative LND-17 showed the most consistent performance, exhibiting binding free energy estimates approaching those obtained for the reference inhibitors nirmatrelvir and ensitrelvir, sustained catalytic pocket occupancy, and energetic contributions involving the catalytic dyad (His41 and Cys145). Additional derivatives, including LNG-04, QND-07, and QNG-20, showed moderate stabilization but lower overall consistency. These findings highlight glycosylated flavonoids as promising scaffolds for future structure-based optimization and provide structural insights to guide experimental validation.

Keywords: SARS-CoV-2; main protease; Mpro; antivirals; flavonoids

Academic Editor: Hermann Stuppner

Received: 6 June 2026
Revised: 20 July 2026
Accepted: 27 July 2026
Published: 31 July 2026

1. Introduction

The COVID-19 pandemic has been one of the most devastating global public health emergencies in recent history, although its impact has been substantially mitigated by advances in epidemiology, virology, and biomedical technologies. While the acute phase

of the crisis has subsided, SARS-CoV-2, responsible for COVID-19, will persist within the human population, likely causing periodic or seasonal respiratory infections. Some of these cases will necessitate hospitalization and, unfortunately, a portion will result in fatalities. The existence of effective vaccines for prevention, along with specific drugs to reduce the mortality risk among the most vulnerable patients, remains crucial. However, the continuous evolution of SARS-CoV-2 may compromise the long-term effectiveness of both preventive and therapeutic strategies.

SARS-CoV-2 belongs to the genus *Betacoronavirus* within the family *Coronaviridae*, which also includes other highly pathogenic viruses such as severe acute respiratory syndrome coronavirus (SARS-CoV) and Middle East respiratory syndrome coronavirus (MERS-CoV). The virion is pleomorphic, predominantly spherical, and enveloped, displaying prominent spike (S) glycoprotein on its surface, along with membrane (M) and envelope (E) proteins. Its genome consists of a positive-sense single-stranded RNA of approximately 30 kb (GenBank accession: NC_045512), encoding two large polyproteins (pp1a and pp1ab), which are proteolytically processed into 16 non-structural proteins (nsp1-nsp16). In addition, four structural proteins and several accessory proteins are expressed from subgenomic RNAs [1–3].

Proteolytic cleavage of these polyproteins is mediated by two viral proteases: the papain-like protease (PLpro, nsp3) and the main protease (3CLpro or Mpro, nsp5). Among these enzymes, Mpro catalyzes 11 of the 14 proteolytic cleavage events within pp1a and pp1ab, whereas PLpro mediates the remaining three cleavages [4,5].

Structurally, Mpro is a highly conserved cysteine endopeptidase. Since the first works on coronaviruses, this protein has garnered significant attention due to its pharmacological potential, particularly with the emergence of clinically relevant viral species like SARS-CoV, MERS-CoV, and SARS-CoV-2 [6–8]. Mpro functions as a homodimer, with each monomer comprising three domains. The catalytic dyad His41 and Cys145 is located in a substrate-binding cleft formed between domains I and II [9]. Due to its essential role in viral replication and the absence of closely related homologues in humans, Mpro represents an attractive and selective antiviral target.

Although vaccination campaigns have substantially reduced COVID-19-related mortality [10–12], SARS-CoV-2 continues to circulate globally, with periodic waves driven by the emergence of new variants. Consequently, effective preventive and therapeutic strategies remain particularly important for high-risk populations, including older adults and individuals with underlying medical conditions [13,14].

Consequently, the development of drugs, particularly antivirals targeting the virus or its components, is imperative. Much of the drug research and development against COVID-19 relies on computational tools, predicting interactions between proteins and small molecules that can serve as enzyme inhibitors, thus streamlining drug research [15–17].

Currently authorized antiviral therapies include molnupiravir, which induces lethal mutagenesis [18], and protease inhibitors such as nirmatrelvir (administered with ritonavir) and ensitrelvir [19,20]. Although these agents remain effective for reducing the risk of severe COVID-19, reports of post-treatment viral rebound and the emergence of resistance-associated mutations underscore the importance of identifying additional Mpro inhibitors with alternative chemical scaffolds [21–25].

Natural products, particularly flavonoids, constitute a chemically diverse class of bioactive compounds with reported antiviral properties. Extracts and fractions obtained from *Taraxacum officinale* and *Urtica dioica* have previously demonstrated in vitro antiviral activity against dengue virus (DENV) [26]. Furthermore, in silico studies suggest that certain flavonoids present in these fractions interact with the NS3 protease of DENV, indicating a potential capacity to target viral proteases and to serve as a structural basis for further optimization [27].

Given the conserved mechanistic relevance of viral proteases as essential mediators of polyprotein processing and viral replication, these findings support the exploration of flavonoid-based compounds against other clinically significant viruses. In this context, the present study aims to employ molecular docking and molecular dynamics (MD) simulations to identify potential inhibitors of the SARS-CoV-2 Mpro protease, a key enzymatic target in the viral replication cycle.

2. Materials and Methods

2.1. Ligand Preparation

Sixteen phytochemicals, including flavonoids and two hydroxylated phenylpropanoid derivatives, were selected as candidate ligands. The initial selection was based on flavonoids previously reported in phytochemical analyses of *Taraxacum officinale* and *Urtica dioica*. To broaden the structural scope of the analysis, additional structurally related flavonoids sharing the same core scaffold and substitution patterns were incorporated, given their reported antiviral properties and potential to interact with viral proteases (Table 1 and Table S1). Additionally, two clinically approved Mpro inhibitors, nirmatrelvir and ensitrelvir, were included as reference ligands for comparative analysis (Table 1). For clarity and consistency, commonly used trivial names were adopted throughout the manuscript. Compound identity was unequivocally defined by the corresponding PubChem Compound Identification (CID) number from the PubChem database (National Center for Biotechnology Information, Bethesda, MD, USA), which served as the primary chemical reference [28]. Files were downloaded in SDF format and converted to the mol2 format using UCSF Chimera 1.14 (Resource for Biocomputing, Visualization, and Informatics, University of California, San Francisco, CA, USA) [29]. The energy minimization was performed in Avogadro 1.1.1 (Avogadro Chemistry Project) [30]. Ligand geometry optimization was conducted employing the MMFF94s force field [31], selected due to its reliable parametrization for small organic molecules and its widespread application in preliminary geometry optimization prior to docking studies. Energy minimization was carried out using the steepest descent algorithm until convergence criteria were achieved, with a minimum of 100 steps per update.

Table 1. PubChem accession code of ligands analyzed in present study.

Compound Name	PubChem CID	Molecule Code
Control ligand		
Nirmatrelvir	CID 155903259	Nirmatrelvir
Ensitrelvir (S-217622)	CID 162533924	Ensitrelvir
Experimental ligand		
3,5-Dicaffeoylquinic acid	CID 6474310	DCA-01
4,5-Dicaffeoylquinic acid	CID 6474309	DCA-09
Kaempferol-3-glucoside	CID 5282102	KFG-19
Luteolin 7,3′-diglucoside	CID 44258089	LND-15
Luteolin 7,4′-diglucoside	CID 44258093	LND-16
Luteolin 3′,4′-diglucoside	CID 44258099	LND-17
Luteolin-7-O-glucoside	CID 5280637	LNG-04
Luteolin-7-O-rutinoside	CID 14032966	LNR-13
Quercetin 3,4′-diglucoside	CID 5320835	QND-07
Quercetin 3,7-diglucoside	CID 10121947	QND-10
Quercetin 3-diglucoside	CID 10211337	QND-11
Quercetin 7,4′-diglucoside	CID 11968881	QND-12
Quercetin 3,5-O-diglucoside	CID 44229098	QND-14
Quercetin 3,3′-diglucoside	CID 44259153	QND-18
Quercetin 3-galactoside	CID 5281643	QNG-20
Quercetin 3-rutinoside	CID 5280805	QNR-05

Shaded rows indicate the compounds with the best characteristics, evaluated in silico, as potential ligands to inhibit SARS-CoV-2 Mpro.

2.2. Selection and Preparation of the Crystallographic Structure of Mpro

Crystallographic structures were obtained from the Research Collaboratory for Structural Bioinformatics (RCSB) Protein Data Bank (PDB) (Rutgers University, Piscataway, NJ, USA) [32]. Structures were screened according to the following criteria: resolution of $\leq$3 Å, absence of mutations in the catalytic site, and acceptable refinement statistics ($R_{work} < R_{free}$ values within standard crystallographic quality thresholds) [33]. Based on these criteria, the structure with PDB ID 6ZRU was selected due to its high resolution and structural completeness of the catalytic dyad (His41 and Cys145) [34].

Protein preprocessing was performed using Chimera 1.14. Co-crystallized ligands, solvent molecules, and DMSO were removed. Protonation states were manually assigned to physiological pH (7.4), and hydrogen atoms were added using the Dock Prep module. Partial charges were assigned according to the AMBER ff14SB force field [35], the most recent force field available in Chimera Dock Prep. Subsequent receptor preparation for AutoDock Vina 1.1.2 (The Scripps Research Institute, La Jolla, CA, USA) and AutoDock FR (ADFR) 1.0 (Molecular Graphics Laboratory, The Scripps Research Institute, La Jolla, CA, USA) followed the charge assignment procedures implemented in their respective docking platforms. The processed structure was saved in mol2 format for docking with AutoDock Vina [36]. For ADFR [37] the structure was separately prepared using AutoDock Tools 1.5.6. Polar hydrogens were added and Kollman charges assigned [38]. The final receptor file was saved in pdbqt format.

2.3. Molecular Docking Assays

The molecular docking simulations were conducted at the National Supercomputing Laboratory of Southeastern Mexico using AutoDock Vina and AutoDock FR. In all simulations the receptor was treated as rigid. For AutoDock Vina calculations, the search space centered on the catalytic cavity using the coordinates x = −17.78, y = −15.49, z = 16.83. Grid box dimensions were set to 30 × 30 × 30 $Å^3$, encompassing the active site region. Docking calculations were performed using an exhaustiveness parameter of 64, while restricting the output to the three highest-ranked binding poses for each ligand. This strategy prioritized the most favorable binding conformations while maintaining computational efficiency [39].

For ADFR calculations, the same grid center coordinates were used x = −17.78, y = −15.49, z = 16.83, while grid dimensions were defined as 26.00 × 29.75 × 21.50 $Å^3$. The grid map (.trg file) was generated using AGFR. Docking simulations were performed using 100 runs and allowing up to 25 million energy evaluations per ligand, generating 500 docking poses per compound. Docking clusters containing at least 10% of the generated poses were considered indicative of recurrent binding modes and were prioritized during pose inspection. This threshold was used as a practical criterion to identify consistently sampled conformations rather than as a statistical cutoff.

To capture both high-ranking candidates and structural diversity, molecular dynamics simulations were performed on eight ligand–protein complexes. Four top-ranked flavonoids (LND-17, LNG-04, QND-07, and QNG-20) were selected based on their docking performance. Baicalein was included as a structurally related flavonoid previously reported as an Mpro inhibitor [40], serving as a comparative reference. In addition, DCA-09, a hydroxylated phenylpropanoid dis-playing the fifth-highest docking score, was incorporated to evaluate the dynamic behavior of a compound representing a distinct chemical scaffold.

2.4. Molecular Dynamics

Molecular dynamics simulations were conducted using the Amber20 and AmberTools21 packages (University of California, San Francisco, CA, USA) [41]. Protein preparation for MD was conducted independently from the docking protocol. The proteins were

parameterized using the ff19SB force field, as recommended in AMBER20 manual, whereas ligand parameters were generated with the General AMBER Force Field (GAFF2) using AM1-BCC atomic charges.

Each protein–ligand complex was solvated in an Optimal Point Charge (OPC) water box with a 10 Å buffer surrounding the system. Sodium and chloride ions were added to neutralize the system. Following energy minimization, systems were gradually heated to 300 K under NVT conditions and equilibrated under NPT conditions at 1 atm. Production simulations were subsequently carried out using Particle Mesh Ewald Molecular Dynamics (PMEMD) with a 2 fs time step. Covalent bonds involving hydrogen atoms were constrained using the SHAKE algorithm, and long-range electrostatic interactions were treated with the Particle Mesh Ewald method using a non-bonded cutoff of 10 Å.

Production simulations were run for 300 ns per system, and three independent replicas were performed to improve sampling and assess trajectory reproducibility. Trajectory analysis was carried out using cpptraj. Relative binding free energies were estimated using the MM-PBSA (Molecular Mechanics Poisson–Boltzmann Surface Area) method implemented in MMPBSA.py. Calculations were performed using an ionic strength of 0.15 M, an internal dielectric constant of 4.0, an external dielectric constant of 78.0, and 100 evenly spaced frames extracted from the final 2000 trajectory frames of each simulation.

MD simulations were performed for eight complexes: including the reference inhibitors nirmatrelvir and ensitrelvir, the four top-ranked flavonoids (LND-17, LNG-04, QND-07, and QND-20), baicalein (reference flavonoid), and DCA-09 as a representative hydroxylated phenylpropanoid. Each system was simulated under identical conditions as described above.

3. Results

3.1. Molecular Docking Using AutoDock Vina

Docking simulations performed with AutoDock Vina (Figure 1A) yielded mean docking scores of -7.42 ± 0.54 kcal/mol for nirmatrelvir and -7.85 ± 0.21 kcal/mol for ensitrelvir. These clinically approved SARS-CoV-2 Mpro inhibitors SARS-CoV-2 Mpro inhibitors were included as reference compounds to provide a qualitative framework for interpreting the docking performance of the evaluated phytochemicals.

Most of the evaluated compounds exhibited docking scores within the range observed for the two reference inhibitors, whereas several derivatives displayed more favorable predicted docking scores. In particular, LND-17 (-8.2 ± 0.22 kcal/mol), LNR-13 (-8.31 ± 0.21 kcal/mol), QND-10 (-8.54 ± 0.30 kcal/mol), and QNR-05 (-8.27 ± 0.18 kcal/mol) showed lower docking scores than both reference compounds, suggesting a favorable predicted interaction with the Mpro active site.

Although docking scores provide only an empirical estimate of ligand–protein interactions and are not quantitative binding free energies, they constitute a useful initial criterion for prioritizing candidate molecules. Consequently, compounds exhibiting favorable docking performance were selected for subsequent analyses using AutoDock FR and molecular dynamics simulations to further evaluate the stability and consistency of their predicted binding modes.

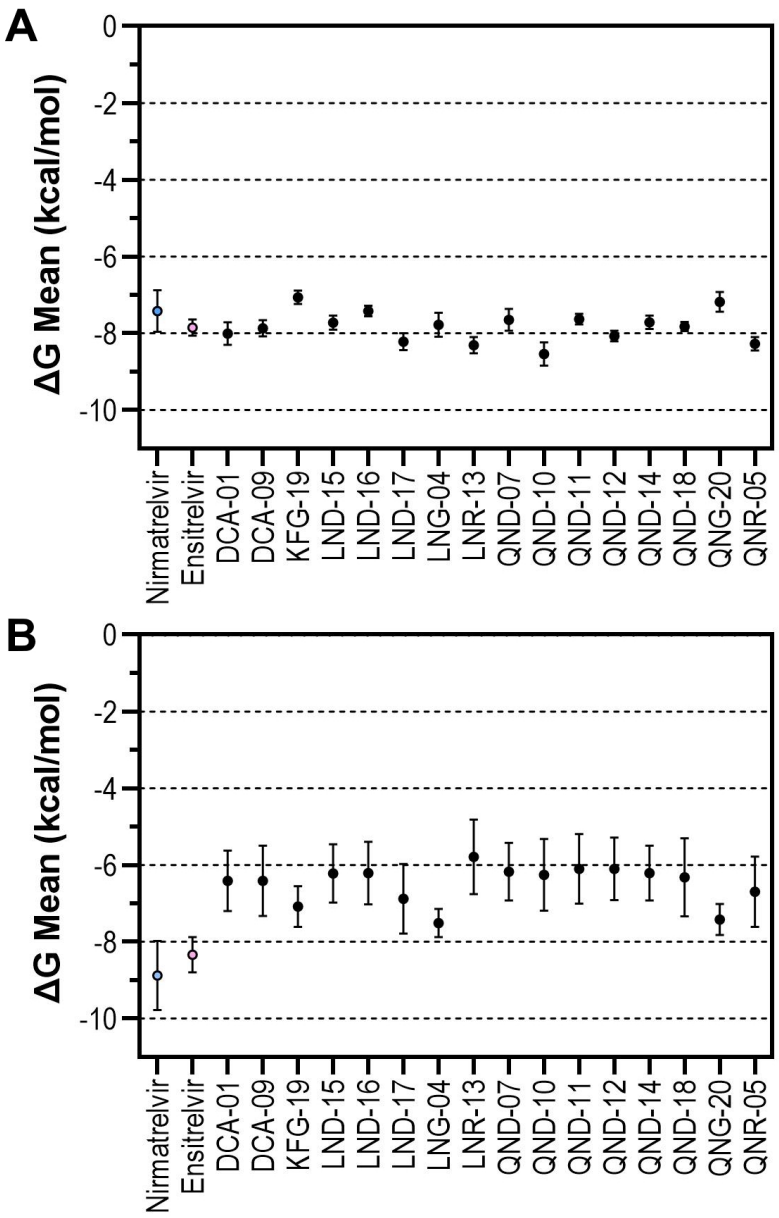

Figure 1. Mean molecular docking scores (kcal/mol) obtained for the evaluated compounds. Values are presented as mean ± SD. (**A**) AutoDock Vina results based on 10 docking poses. (**B**) ADFR results based on 500 docking poses. Nirmatrelvir (blue dot) and ensitrelvir (pink dot) were included as reference compounds for comparison.

3.2. Molecular Docking Using ADFR

In a parallel docking analysis using ADFR (Figure 1B), 500 interaction decoys per ligand were generated and grouped into clusters based on pose similarity (Root Mean Square Deviation, RMSD < 10 Å). Unlike AutoDock Vina, which reports a limited number of top-ranked poses, ADFR samples a broader conformational space, allowing the recurrence of similar binding modes to be evaluated through cluster analysis.

Mean docking scores were calculated from all 500 generated poses for each ligand. The reference inhibitors nirmatrelvir and ensitrelvir yielded average docking scores of −8.88 ± 0.90 kcal/mol and −8.34 ± 0.46 kcal/mol, respectively. The evaluated flavonoids displayed mean docking scores ranging from approximately −5 and −8 kcal/mol, with the five more favorable values corresponding to LNG-04 (−7.50 ± 0.37 kcal/mol), QNG-20

(−7.42 ± 0.40 kcal/mol), KFG-19 (−7.08 ± 0.53 kcal/mol), LND-17 (−6.88 ± 0.90 kcal/mol), and QNR-05 (−6.70 ± 0.92 kcal/mol).

An important feature of ADFR is the identification of recurrent binding modes through pose clustering. The proportion of poses contained within the largest cluster was used as an indicator of conformational convergence and reproducibility. The largest clusters comprised 127 of 500 poses for nirmatrelvir and 107 of 500 poses for ensitrelvir. Several flavonoids exhibited even greater clustering, including QNG-20 (273/500), KFG-19 (223/500), LND-17 (216/500), LNG-04 (203/500), LND-16 (176/500), and QND-07 (133/500). For LNG-04 and LND-16, the most populated cluster also contained the lowest-energy docking pose (Table S2), suggesting structural convergence toward a stable binding orientation.

Candidate selection for molecular dynamics simulations was based on an integrative assessment that considered docking performance in AutoDock Vina, mean docking scores in ADFR, recurrence of binding poses (largest cluster > 100/500 decoys), convergence between the lowest-energy pose and the most populated cluster and visual inspection of interactions within the catalytic dyad (His41–Cys145) and neighboring active-site residues. Under this integrative approach, four ligands emerged as the most consistent candidates: LND-17 (Figure 2C), LNG-04 (Figure 2D), QND-07 (Figure 2E), and QNG-20 (Figure 2F). Although QND-10 and QNR-05 achieved more favorable docking scores in AutoDock Vina, they showed lower conformational convergence or clustering robustness in ADFR. Conversely, QND-07 and LNG-04 exhibited highly recurrent binding modes despite not ranking among the top-scoring compounds in AutoDock Vina, suggesting greater consistency across the two docking approaches.

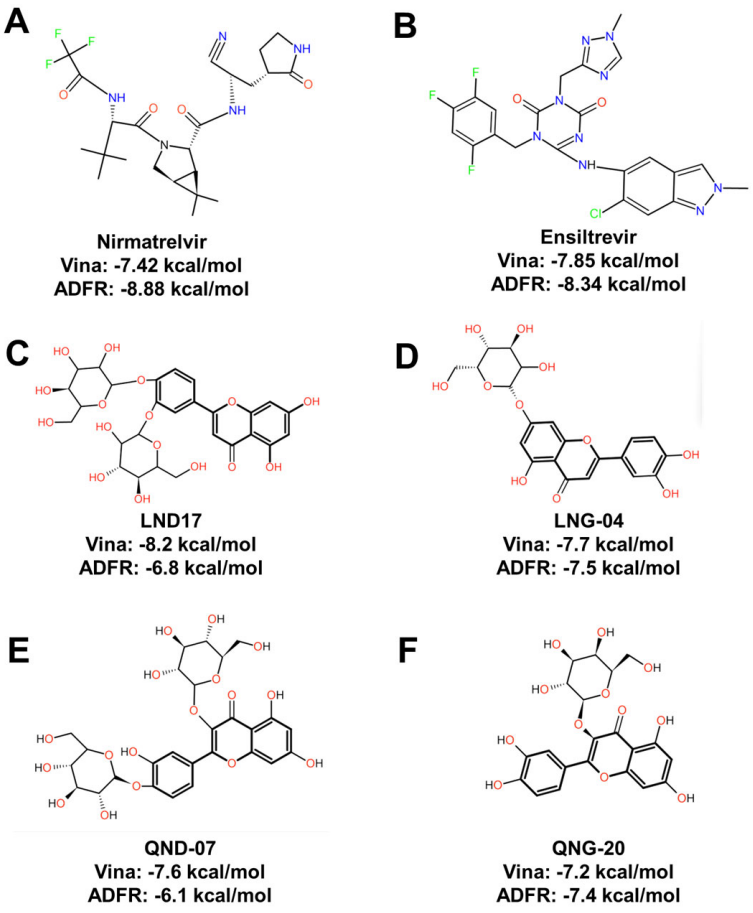

Figure 2. Chemical structure of notable ligands. (**A**,**B**) Reference ligands. (**C**–**F**) Experimental ligands with the flavonoid core highlighted. The average ΔG calculated in each molecular docking program is indicated under each structure.

3.3. Receptor–Ligand Interactions in Molecular Docking Models

For interaction analysis, the top-ranked docking pose obtained with AutoDock Vina and the representative structure of the most populated cluster generated by ADFR were selected for each ligand. The representative ADFR structures analyzed corresponded to the lowest-energy conformations within their respective dominant clusters (Table S2). The catalytic pocket of SARS-CoV-2 Mpro was analyzed according to its structurally defined subsites S1′, S1, S2, and S4, as described in crystallographic studies (Table 2). Figure 3 illustrates the selected docking models, with subsites color-coded to facilitate structural interpretation. Only these structurally established subsites (S1′, S1, S2, and S4) were considered in the interaction analysis. The four selected flavonoids are arranged in rows, whereas the corresponding 3D and 2D models are arranged in columns.

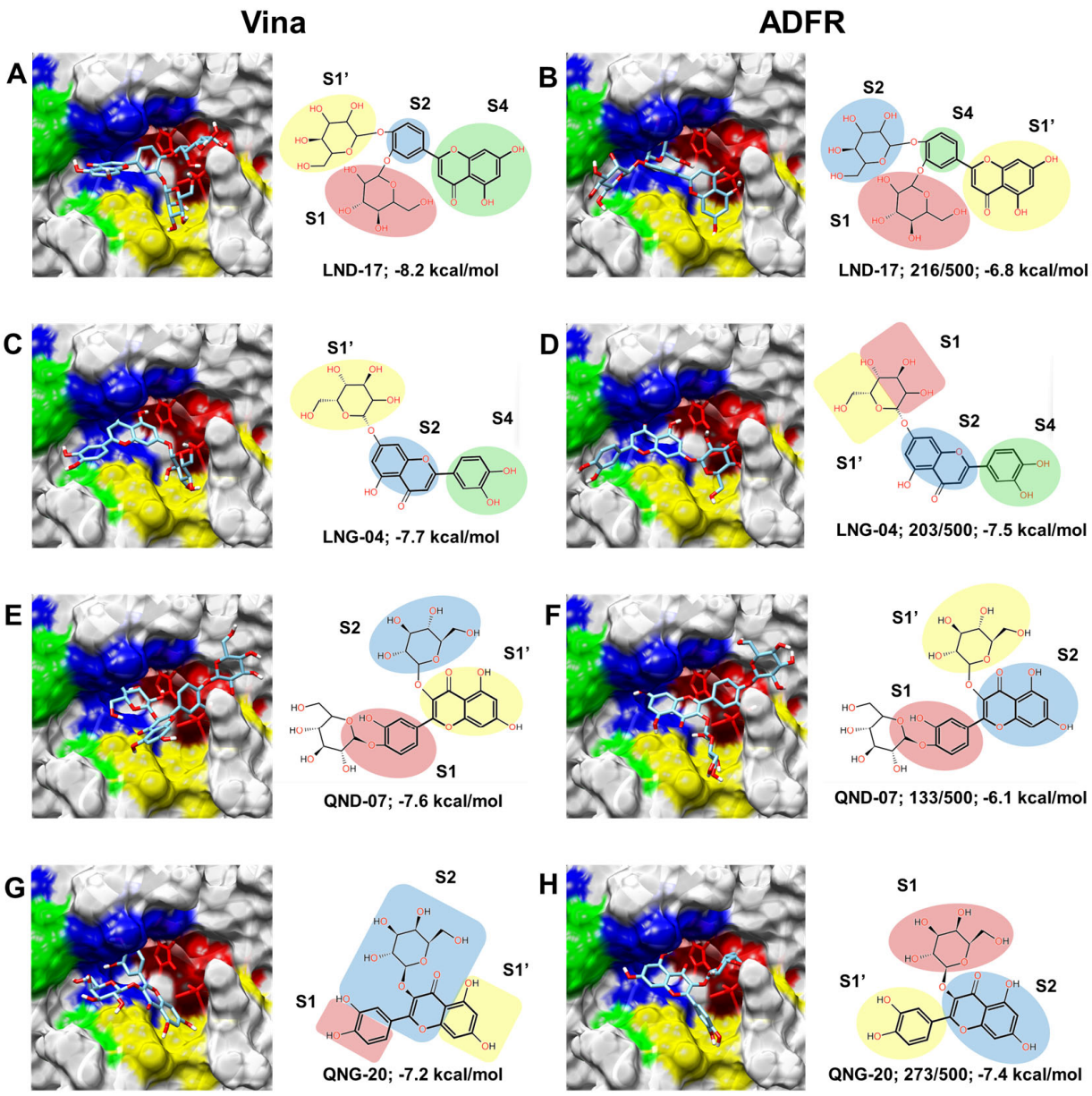

Figure 3. Receptor—ligand interactions of featured flavonoids. For each ligand, the model with the most negative ΔG obtained with Autodock Vina (**A**,**C**,**E**,**G**), and the most frequent conformation in ADFR (**B**,**D**,**F**,**H**) is shown. In the 3D representations of the models, the regions of the catalytic cavity are delimited by colors: S1: red; S1′: yellow; S2: blue; S4: green. In the 2D representations, it is specified which part of the molecule interacts with the catalytic cavity region.

Table 2. Structural features and preferred substrate residues of the SARS-CoV-2 Mpro substrate-binding subsites.

Subsites	Major Residues	Preferred Substrate Residues
S1′	L27, H41, C145	Ala, Ser, Gly, Asn
S1	F140, G143, S144, H163, E166	Gln
S2	H41, M49, M165, V186, D187, R188, Q189	Leu, Phe, Met, Val
S4	M165, L167, Q189, T190, A191	Ala, Val, Pro, Thr

Colors indicate the same substrate-binding subsites depicted in Figure 3.

For LND-17 (Figure 3A,B) differences between Vina and ADFR models are attributable to ligand orientation within the catalytic cavity. In both docking approaches, LND-17 occupies regions corresponding primarily to S1, S2, and S4, with additional contacts extending toward S1′. This ligand establishes up to six hydrogen bonds involving Thr26, His41, Asn142, Phe140, Leu141, Glu166, Arg188, Thr190, and Gln192. Notably, hydrogen bonding with His41 places the ligand in proximity to the catalytic dyad. Hydrophobic interactions are observed with Thr25, Leu27, Met49, Cys145, His163, His172, Met165, and Gln189, potentially contributing to ligand stabilization within the binding cleft.

In the case of LNG-04 (Figure 3C,D), both docking programs predict distinct ligand conformations; however, the binding location remains consistent within subsites S1, S2, and S4. The glucose moiety extends toward the solvent-exposed region while the flavonoid core occupies the central pocket. Up to five hydrogen bonds are formed, primarily involving Phe140, Ser144 and Gln192. Recurrent hydrophobic contacts include His41, Leu141, His163, His164, Met165, Glu166, Leu167, Pro168, Arg188 and Gln189. Although LNG-04 does not form a hydrogen bond directly with His41, it maintains hydrophobic interactions with residues lining the catalytic region, including Cys145.

Analyzing QND-07 (Figure 3E,F) reveals occupation of subsites S1, S1′, and S2 in Vina and ADFR. This ligand demonstrates the highest hydrogen bonding capacity among the selected flavonoids, forming up to nine simultaneous hydrogen bonds involving His41, Phe140, Leu141, Asn142, Ser144, His164, Glu166 and Thr190. Hydrophobic interactions are observed with Met49, Cys145, His163, Met165, Asp187, Arg188 and Gln189. The hydrogen bond with His41 further supports positioning within the catalytic region.

For QNG-20 (Figure 3G,H), both docking programs predict highly similar orientations, indicating structural consistency. The ligand occupies subsites S1, S1′, and S2, maintaining a stable positioning across both methodologies. Five hydrogen bonds are observed, primarily involving Ser144, Leu141, Arg188 and Thr190. Hydrophobic interactions occur with Met49, Phe140, Cys145, His163, Met165, Glu166, Asp187 and Gln189. The similar orientations predicted by both docking approaches support the consistency of the proposed binding mode.

Among the selected flavonoids, LND-17 and QND-07 establish hydrogen bonds with His41, a residue belonging to the catalytic dyad (His41-Cys145). LNG-04 and QNG-20 interact with His41 and Cys145 predominantly through hydrophobic contacts. All four ligands established multiple interactions with residues lining the S1 and S2 subsites, while hydrogen bonds were mainly distributed within the S1 and S4 regions and hydrophobic contacts predominated in S2. Overall, the interaction patterns predicted by both docking approaches supported the selection of these four flavonoids for subsequent molecular dynamics simulations.

3.4. Receptor–Ligand Stability During MD

The RMSD profiles (Figure 4) revealed distinct dynamic behaviors among the evaluated protein–ligand complexes. Nirmatrelvir exhibited the highest structural stability, maintaining low-amplitude deviations throughout the 300 ns simulations (Video S1). Ensitrelvir

showed moderate fluctuations during the intermediate stage but remained consistently posicioned within the catalytic cavity (Video S2).

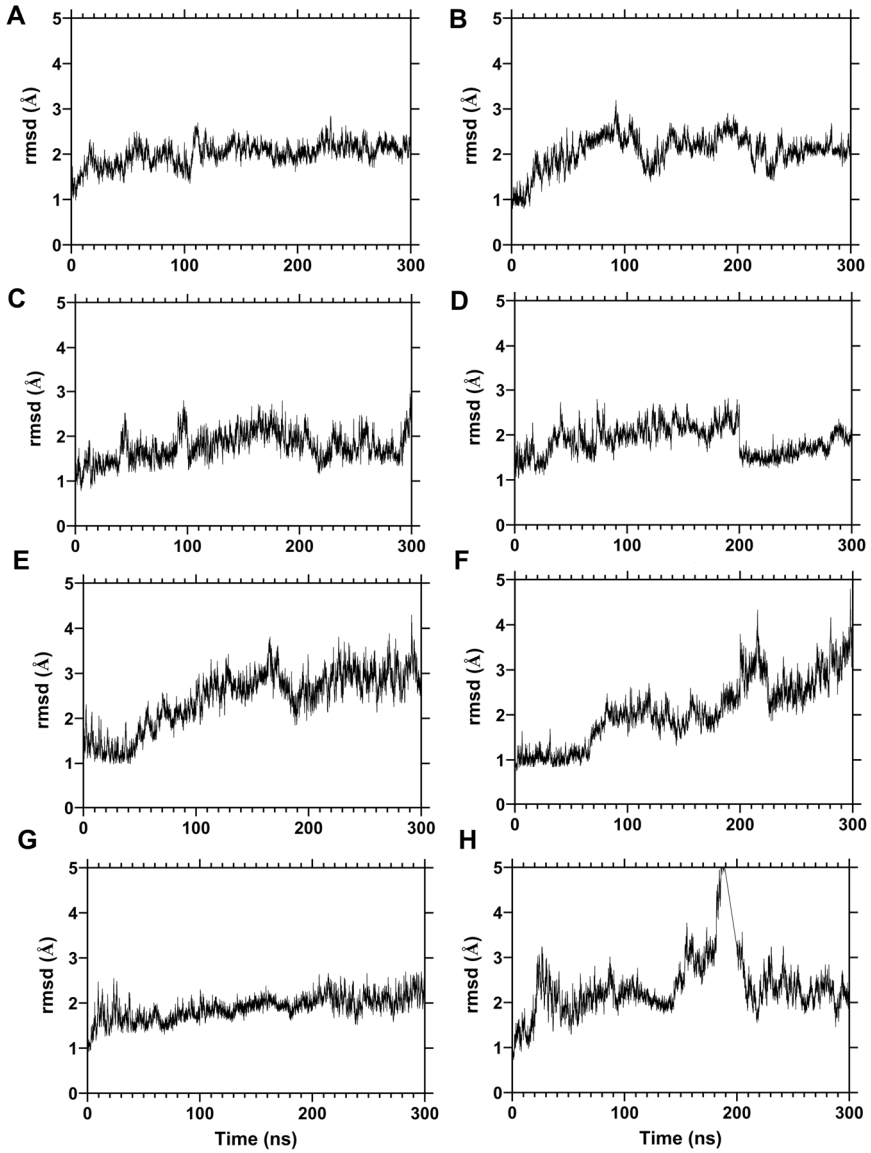

Figure 4. Root mean square deviation (RMSD) of the receptor backbone during molecular dynamics simulations. Panels correspond to (**A**) Nirmatrelvir, (**B**) Ensitrelvir, (**C**) LND-17, (**D**) LNG-04, (**E**) QND-07, (**F**) QND-20, (**G**) Baicalein, and (**H**) DCA-09.

Among the flavonoids selected from docking, LND-17 and QNG-20 demonstrated stability profiles comparable to the reference inhibitors, maintaining sustained positioning within the active site (Videos S3 and S4). In the case of LND-17, remained consistently positioned within the catalytic pocket, with only minor displacement of the flavonoid core over time. LNG-04 displayed two distinguishable stability regimes (Video S5), suggesting conformational rearrangements within the binding pocket while maintaining continuous occupancy of the catalytic site.

In contrast, QND-07 showed increased conformational mobility, reflected by higher RMSD fluctuations and progressive positional adjustments within the binding pocket (Video S6). Baicalein exhibited a similar dynamic behavior, suggesting that this flavonoid scaffold may allow greater flexibility within the catalytic cavity. DCA-09 presented the highest sustained deviations among all systems, indicating lower dynamic stability relative to the other ligands.

Despite these differences in conformational behavior, none of the protein–ligand complexes exhibited dissociation from the catalytic cavity during the simulations.

3.5. Mpro Flexibility Profiles During MD (RMSF)

The RMSF analysis (Figure 5) revealed similar flexibility patterns among all simulated systems, particularly in residues 45–50, which form part of the S4 subsite. This region exhibited greater flexibility in the QND-07 and baicalein complexes than in those containing LND-17, QNG-20, or the reference inhibitors, consistent with the higher conformational mobility observed in their RMSD trajectories. Terminal residues displayed higher flexibility in all systems; however, due to their spatial separation from the catalytic dyad (His41 and Cys145), these fluctuations are unlikely to directly affect catalytic function. Among the evaluated ligands, DCA-09 induced broader fluctuation patterns across multiple regions, reinforcing its comparatively weaker stabilization profile and aligning with its dynamic behavior observed in trajectory analysis.

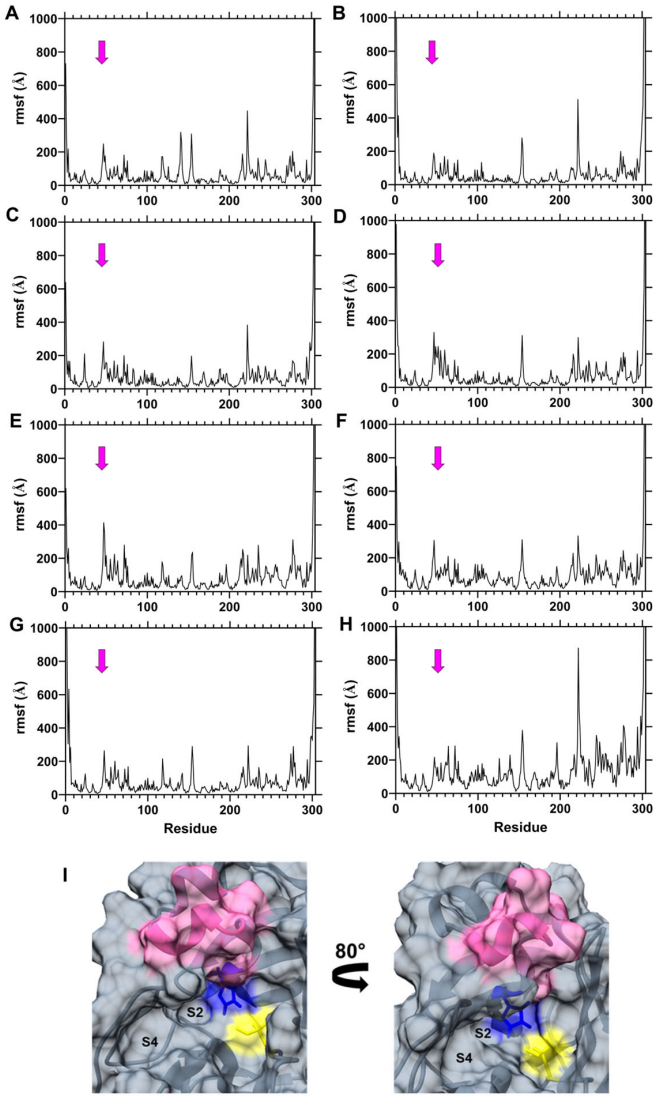

Figure 5. Trajectory of the receptor–ligand complexes. The trajectories show the average three repetitions of the simulation. For each repetition, 300 ns were simulated. Panels correspond to (**A**) Nirmatrelvir, (**B**) Ensitrelvir, (**C**) LND-17, (**D**) LNG-04, (**E**) QND-07, (**F**) QND-20, (**G**) Baicalein, and (**H**) DCA-09. The x-axis represents simulation time in nanoseconds. The arrow indicates amino acids 45–50, whose RMSF is notable for its proximity to the catalytic cavity. (**I**) Visualization of amino acids 45–50 (pink). For reference, His41 is marked in blue and Cys145 is marked in yellow.

3.6. Relative Binding Free Energy Analysis (MM-PBSA)

The MM-PBSA binding free energy estimate (Figure 6) were consistent with the dynamic behavior observed. Among the reference compounds, nirmatrelvir and ensitrelvir exhibited the most favorable free energies (−33.18 and −32.52 kcal/mol, respectively). Baicalein showed a substantially less favorable binding free energy estimate (−21.35 kcal/mol), consistent with its greater conformational mobility observed in the RMSD and RMSF analyses. Similar energetic profiles were obtained for QND-07 (−21.94 kcal/mol) and QNG-20 (−20.43 kcal/mol), whereas DCA-09 exhibited an intermediate binding energy (−24.36 kcal/mol) despite displaying comparatively higher conformational fluctuations throughout the simulations.

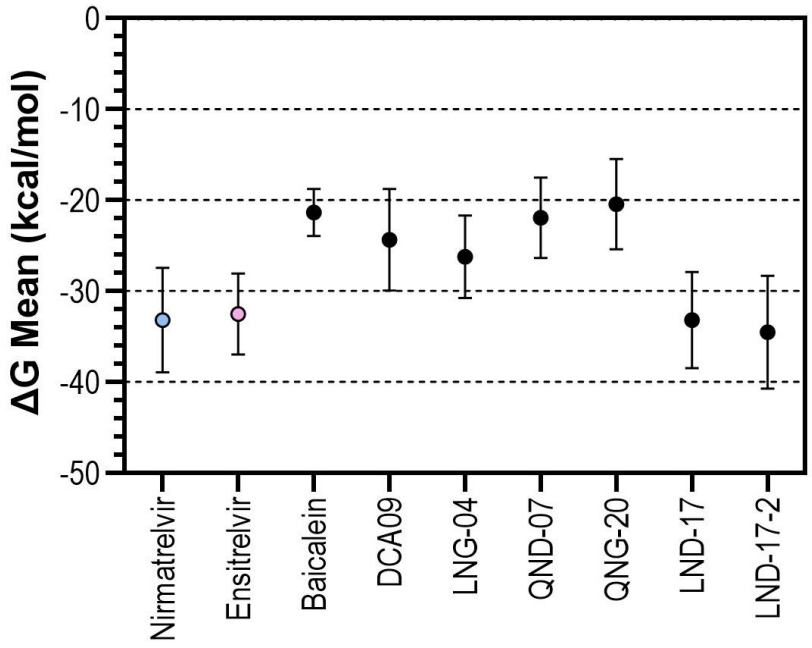

Figure 6. MM-PBSA binding free energy estimates (kcal/mol) calculated from 300 ns molecular dynamics simulations. Values are presented as mean ± SD from three independent simulations. Nirmatrelvir (boue dot) and ensitrelvir (pink dot) were included as reference compounds for comparison.

Notably, LND-17 exhibited the most favorable energetic profile, with a binding free energy estimate (−33.2 kcal/mol), comparable to those obtained for the reference inhibitors. This result was consistent with its stable RMSD profile, reduced residue flexibility, and persistent occupancy of the catalytic pocket throughout the simulations. Visual inspection of the trajectories (Video S3), indicated that structural rearrangements were primarily limited to the orientation of the glycosidic substituent, whereas the luteolin scaffold remained stably anchored within the catalytic cavity, maintaining interactions across the S2 and S4 subsites.

To further elucidate the energetic basis of this favorable energetic profile, a per-residue MM-PBSA decomposition analysis was performed (Figure 7). The largest energetic contributions originated from His41, Cys145, Met165, Glu166, Leu167, Val186, and Gln189. Notably, His41 and Cys145 constitute the catalytic dyad of Mpro, whereas Glu166 and Gln189 play key roles in defining the S1 and S4 subsites. These results indicate that the binding free energy of LND-17 is distributed across both catalytic and substrate-recognition residues rather than being dominated by a single interaction, supporting a balanced binding mode within the catalytic cleft.

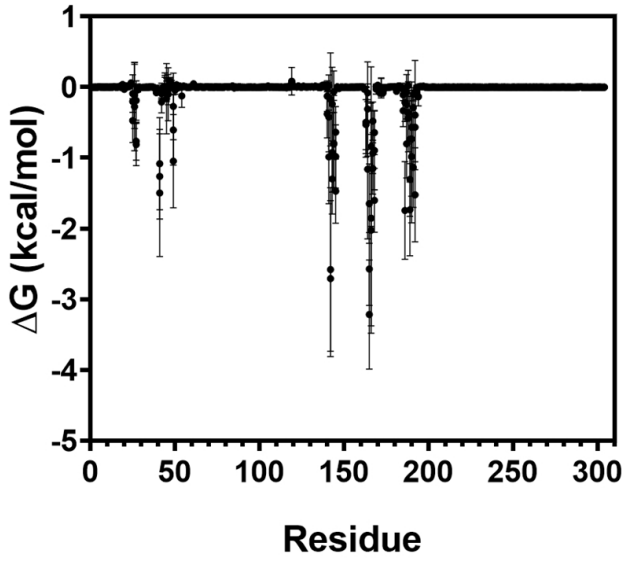

Figure 7. Per residue contribution to binding affinity from MMPSA. Energetic contributions to LND-17 are shown. The values were obtained from three repetitions of the MD.

Based on these observations, a rational derivative of LND-17 was designed by introducing an additional glycosyl substituent into the luteolin scaffold, generating LND-17-2 (Table S1). The modification was intended to increase subsite occupancy and promote additional polar interactions within the binding pocket. However, the resulting compound exhibited only a marginal improvement in the estimated binding free energy (−34.52 kcal/mol), suggesting that further glycosylation provides limited energetic benefit within the evaluated binding model. Together, these findings identify LND-17 as the flavonoid with the most favorable combination of dynamic stability and predicted binding affinity among the compounds evaluated.

4. Discussion

The present study combined molecular docking, long-timescale molecular dynamics simulations (300 ns), and MM-PBSA free energy calculations to identify substituted flavonoids with inhibitory potential against the SARS-CoV-2 Mpro. While docking served as an initial screening tool, dynamic and energetic refinement identified LND-17 as the most structurally and energetically consistent candidate.

Previous benchmarking studies [42,43] have demonstrated that SARS-CoV-2 Mpro remains a challenging target for docking-based virtual screening, as docking scores alone do not consistently predict stable binding modes or inhibitory activity. Consequently, relying exclusively on docking may lead to false-positive prioritization of candidate compounds. To address this limitation, we adopted a hierarchical computational workflow in which a focused library of flavonoid derivatives was evaluated using two complementary docking programs, followed by extended molecular dynamics simulations and MM-PBSA binding free energy analyses to refine ligand selection. Nirmatrelvir and ensitrelvir, two approved Mpro inhibitors, were included as reference compounds throughout the computational workflow to provide qualitative benchmarks for comparison.

Although AutoDock Vina predicted favorable docking scores for multiple flavonoids, the molecular dynamics simulations revealed that not all docking-favored compounds maintained stable binding throughout the simulations. This highlights the importance of complementing docking with dynamic analyses when evaluating Mpro inhibitors. Among all evaluated ligands, LND-17 consistently exhibited the most favorable profile, combining stable occupancy of the catalytic pocket, limited conformational fluctuations, and a MM-

PBSA binding free energy estimate comparable to those obtained for the reference inhibitors. Furthermore, per-residue energy identified substantial energetic contributions from His41 and Cys145, the catalytic dyad, together with Glu166, Met165, Leu167, Val186, and Gln189, which define key subsites. Rather than depending on a single dominant interaction, these results indicate that the stability of LND-17 arises from a balanced interaction network distributed across the catalytic cavity.

A rational optimization strategy was applied to LND-17 by introducing an additional glycosidic moiety to generate LND-17-2. Although this modification produced a slightly more favorable MM-PBSA binding free energy estimate, the improvement was modest and was not accompanied by enhanced dynamic stability. These observations suggest that LND-17 may already achieve near-optimal occupancy of the catalytic cavity and that simple glycosyl extension does not necessarily increase affinity. Rather, these findings indicate possible steric and hydrogen-bonding saturation within the active site, providing structural insight for future design strategies that may require alternative functional groups rather than additional glycosidic units.

Interestingly, DCA-09 exhibited a distinct flexibility profile compared with the flavonoid derivatives evaluated. This behavior may be associated with its phenylpropanoid scaffold, which differs substantially from the flavonoid framework and may provide greater conformational freedom, potentially related, at least in part, to a higher number of rotatable bonds. However, the specific structural determinants underlying this behavior were beyond the scope of the present study and warrant further investigation.

Currently, no flavonoid-based anti-COVID-19 treatment is authorized, although clinical investigations have reported heterogeneous outcomes. For example, quercetin supplementation showed no significant difference in clinical progression in a Turkish cohort [44], whereas a study conducted in Pakistan reported accelerated recovery among patients receiving quercetin supplementation [45]. A 2023 systematic review concluded that quercetin may reduce hospitalization and mortality risks, although variability among studies remains substantial [46]. Luteolin has been proposed primarily for post-COVID-19 neurological or neuropathic complications, likely due to its immunomodulatory and anti-inflammatory properties [47,48].

Beyond SARS-CoV-2, quercetin has demonstrated antiviral activity against herpes simplex virus, hepatitis B and C viruses, influenza virus, enterovirus, Coxsackie virus, HIV-1, and filoviruses such as Ebola [49], although its precise molecular mechanisms remain incompletely characterized. Similarly, luteolin exhibits antiviral effects against influenza, hepatitis viruses, enteroviruses, papillomaviruses, chikungunya virus, and several plant viruses [50]. Both flavonoids have been evaluated against coronaviruses; Ryu et al. demonstrated inhibition of SARS-CoV Mpro by quercetin and luteolin [51]. For SARS-CoV-2, quercetin has been proposed as a 3CL protease inhibitor [52], while luteolin may interfere with viral entry through interaction with the spike protein [53], supported primarily by in silico analyses. Both compounds have also been reported to inhibit viral RNA polymerase and protease activity [54,55].

However, studies focusing on structurally substituted derivatives of these flavonoids remain limited. The present findings suggest that glycosylated derivatives such as LND-17 may exhibit distinct interaction patterns, achieving direct engagement with catalytic residues and dynamic stability comparable to approved antivirals. This distinction is critical: rather than evaluating flavonoids as generic nutraceuticals, the present work supports their development as rationally optimized antiviral scaffolds. Given the immunopathogenic component of severe viral infections, including COVID-19, influenza, and dengue, characterized by excessive proinflammatory cytokine production [56–58], flavonoids derivatives combining direct antiviral activity with anti-inflammatory properties may represent attractive candidates for further development [59–61].

Considering the ongoing evolution of SARS-CoV-2 variants, continued identification of structurally diverse inhibitors remains essential. The computational workflow employed in the present study demonstrates that integrating complementary docking approaches with extended molecular dynamics simulations and MM-PBSA analyses provides a rigorous strategy for prioritizing candidate inhibitors before experimental evaluation. Nonetheless, enzymatic inhibition assays, cellular antiviral models, pharmacokinetic characterization and toxicity will be required to confirm the therapeutic potential of LND-17 and related derivatives.

5. Conclusions

The hierarchical computational workflow employed in this study, integrating complementary docking approaches with long-timescale molecular dynamics simulations and MM-PBSA binding free energy analyses, enabled the identification of promising flavonoid derivatives targeting SARS-CoV-2 Mpro. Among the evaluated compounds, LND-17 exhibited the most favorable overall computational profile, combining stable occupancy of the catalytic pocket with binding free energy estimates comparable to those obtained for the reference inhibitors. Although the rationally designed derivative LND-17-2 produced only modest energetic improvements, the results provide useful insights for future structure-based optimization of glycosylated flavonoids. Overall, this study supports LND-17 as a promising candidate for further investigation and highlights the value of integrating docking, molecular dynamics, and free energy calculations for computational lead prioritization. Experimental validation will be essential to confirm its antiviral activity and therapeutic potential.

Supplementary Materials: Supporting documentation is available at http://doi.org/10.6084/m9.figshare.28373492. Table S1. Chemical structure of ligands analyzed in this study. Table S2. Molecular docking results in supercomputing. Video S1. Mpro protease domains 1 (bottom) and 2 (top) non-covalently bound to nirmatrelvir (file name control). Three trajectories of 300 ns are concatenated together to show the general evolution of the system. Although the simulation was run in explicit solvent, no water molecules or ions are shown. Secondary structures are indicated as yellow (β sheets), and magenta (α helices). Video S2. Mpro protease domains 1 (bottom) and 2 (top) non-covalently bound ensitrelvir (file name S-21622-MPEG1). Three trajectories of 300 ns are concatenated together to show the general evolution of the system. Although the simulation was run in explicit solvent, no water molecules or ions are shown. Secondary structures are indicated as yellow (β sheets), and magenta (α helices). Video S3. Mpro protease domains 1(bottom) and 2 (top) non-covalently bound LND-17 (coded L34G-MPEG1). Three trajectories of 300 ns are concatenated together to show the general evolution of the system. Although the simulation was run in explicit solvent, no water molecules or ions are shown. Secondary structures are indicated as yellow (β sheets), and magenta (α helices). Video S4. Mpro protease domains 1 (bottom) and 2 (top) non-covalently bound QNG-20 (coded Q3C). Three trajectories of 300 ns are concatenated together to show the general evolution of the system. Although the simulation was run in explicit solvent, no water molecules or ions are shown. Secondary structures are indicated as yellow (β sheets), and magenta (α helices). Video S5. Mpro protease domains 1 (bottom) and 2 (top) non-covalently bound LNG-04 (coded L7OG-MPEG1). Three trajectories of 300 ns are concatenated together to show the general evolution of the system. Although the simulation was run in explicit solvent, no water molecules or ions are shown. Secondary structures are indicated as yellow (β sheets), and magenta (α helices). Video S6. Mpro protease domains 1 (bottom) and 2 (top) non-covalently bound QND-07 (coded Q34C). Three trajectories of 300 ns are concatenated together to show the general evolution of the system. Although the simulation was run in explicit solvent, no water molecules or ions are shown. Secondary structures are indicated as yellow (β sheets), and magenta (α helices).

Author Contributions: Conceptualization, L.D.-R., I.H.-C. and G.S.-L.; methodology, G.F.-T., L.D.-R., L.M.-D., J.R.-L. and I.H.-C.; software, G.F.-T., L.D.-R. and P.C.-H.; validation, L.D.-R., L.M.-D., J.R.-L., F.D. and I.H.-C.; formal analysis, L.D.-R., L.M.-D., I.H.-C. and G.S.-L.; investigation, G.F.-T.,

J.H., J.R.-L., P.C.-H. and F.D.; writing—original draft preparation, G.F.-T., L.M.-D. and G.S.-L.; writing—review and editing, G.F.-T. and G.S.-L.; visualization, G.F.-T., L.D.-R. and L.M.-D.; supervision, P.C.-H., J.R.-L., J.H., I.H.-C. and G.S.-L.; project administration, I.H.-C., J.H. and G.S.-L.; funding acquisition, G.S.-L. All authors have read and agreed to the published version of the manuscript.

Funding: This research was funded by Instituto Mexicano del Seguro Social, grant number R-2020-785-085 and Consejo Nacional de Humanidades Ciencias y Tecnologías, grant number PCC-2022/319268. G. Flores-Tlalpa was supported by Consejo Nacional de Humanidades Ciencias y Tecnologías (744943).

Institutional Review Board Statement: Not applicable.

Informed Consent Statement: Not applicable.

Data Availability Statement: Supporting documentation is available at http://doi.org/10.6084/m9.figshare.28373492.

Acknowledgments: The authors thank the National Supercomputing Laboratory of Southeast Mexico, for the computational resources and technical assistance.

Conflicts of Interest: The authors declare no conflicts of interest.

Abbreviations

The following abbreviations are used in this manuscript:

Mpro/3CL	SARS-CoV-2 main protease
nsp	Non-structural proteins
ADFR	AutoDock FR
RMSF	Root mean square fluctuations
MD	Molecular dynamics
MMPBSA	Molecular Mechanics Poisson–Boltzmann Surface Area

References

1. Zhu, N.; Zhang, D.; Wang, W.; Li, X.; Yang, B.; Song, J.; Zhao, X.; Huang, B.; Shi, W.; Lu, R.; et al. A Novel Coronavirus from Patients with Pneumonia in China, 2019. *N. Engl. J. Med.* **2020**, *382*, 727–733. [CrossRef] [PubMed]
2. Rahimi, A.; Mirzazadeh, A.; Tavakolpour, S. Genetics and genomics of SARS-CoV-2: A review of the literature with the special focus on genetic diversity and SARS-CoV-2 genome detection. *Genomics* **2021**, *113*, 1221–1232. [CrossRef] [PubMed]
3. Rosas-Murrieta, N.H.; Rodriguez-Enriquez, A.; Herrera-Camacho, I.; Millan-Perez-Pena, L.; Santos-Lopez, G.; Rivera-Benitez, J.F. Comparative Review of the State of the Art in Research on the Porcine Epidemic Diarrhea Virus and SARS-CoV-2, Scope of Knowledge between Coronaviruses. *Viruses* **2024**, *16*, 238. [CrossRef] [PubMed]
4. V'Kovski, P.; Kratzel, A.; Steiner, S.; Stalder, H.; Thiel, V. Coronavirus biology and replication: Implications for SARS-CoV-2. *Nat. Rev. Microbiol.* **2021**, *19*, 155–170. [CrossRef] [PubMed]
5. Knoops, K.; Kikkert, M.; Worm, S.H.; Zevenhoven-Dobbe, J.C.; van der Meer, Y.; Koster, A.J.; Mommaas, A.M.; Snijder, E.J. SARS-coronavirus replication is supported by a reticulovesicular network of modified endoplasmic reticulum. *PLoS Biol.* **2008**, *6*, e226. [CrossRef] [PubMed]
6. Ziebuhr, J.; Heusipp, G.; Siddell, S.G. Biosynthesis, purification, and characterization of the human coronavirus 229E 3C-like proteinase. *J. Virol.* **1997**, *71*, 3992–3997. [CrossRef] [PubMed]
7. Thiel, V.; Ivanov, K.A.; Putics, A.; Hertzig, T.; Schelle, B.; Bayer, S.; Weissbrich, B.; Snijder, E.J.; Rabenau, H.; Doerr, H.W.; et al. Mechanisms and enzymes involved in SARS coronavirus genome expression. *J. Gen. Virol.* **2003**, *84*, 2305–2315. [CrossRef] [PubMed]
8. Yanez, O.; Osorio, M.I.; Uriarte, E.; Areche, C.; Tiznado, W.; Perez-Donoso, J.M.; Garcia-Beltran, O.; Gonzalez-Nilo, F. In Silico Study of Coumarins and Quinolines Derivatives as Potent Inhibitors of SARS-CoV-2 Main Protease. *Front. Chem.* **2020**, *8*, 595097. [CrossRef] [PubMed]
9. Jin, Z.; Du, X.; Xu, Y.; Deng, Y.; Liu, M.; Zhao, Y.; Zhang, B.; Li, X.; Zhang, L.; Peng, C.; et al. Structure of M(pro) from SARS-CoV-2 and discovery of its inhibitors. *Nature* **2020**, *582*, 289–293. [CrossRef] [PubMed]
10. Tseng, H.F.; Ackerson, B.K.; Sy, L.S.; Tubert, J.E.; Luo, Y.; Qiu, S.; Lee, G.S.; Bruxvoort, K.J.; Ku, J.H.; Florea, A.; et al. mRNA-1273 bivalent (original and Omicron) COVID-19 vaccine effectiveness against COVID-19 outcomes in the United States. *Nat. Commun.* **2023**, *14*, 5851. [CrossRef] [PubMed]

11. Dominguez-Ramirez, L.; Sosa-Jurado, F.; Diaz-Sampayo, G.; Solis-Tejeda, I.; Rodriguez-Perez, F.; Pelayo, R.; Santos-Lopez, G.; Cortes-Hernandez, P. Age and Comorbidities as Risk Factors for Severe COVID-19 in Mexico, before, During and After Massive Vaccination. *Vaccines* **2023**, *11*, 1676. [CrossRef] [PubMed]
12. Sarwar, M.U.; Waasia, F.Z.; Aloqbi, A.A.; Alandiyjany, M.; Alqahtani, R.M.; Hafiz, L.A.; Shamlan, G.; Albreiki, M. Real-world effectiveness of the inactivated COVID-19 vaccines against variant of concerns: Meta-analysis. *J. Infect. Public Health* **2024**, *17*, 245–253. [CrossRef] [PubMed]
13. Dite, G.S.; Murphy, N.M.; Allman, R. An integrated clinical and genetic model for predicting risk of severe COVID-19: A population-based case-control study. *PLoS ONE* **2021**, *16*, e0247205. [CrossRef] [PubMed]
14. Zsichla, L.; Muller, V. Risk Factors of Severe COVID-19: A Review of Host, Viral and Environmental Factors. *Viruses* **2023**, *15*, 175. [CrossRef] [PubMed]
15. Tao, X.; Huang, Y.; Wang, C.; Chen, F.; Yang, L.; Ling, L.; Che, Z.; Chen, X. Recent developments in molecular docking technology applied in food science: A review. *Int. J. Food Sci. Technol.* **2020**, *55*, 33–45. [CrossRef]
16. Li, D.; Luan, J.; Zhang, L. Molecular docking of potential SARS-CoV-2 papain-like protease inhibitors. *Biochem. Biophys. Res. Commun.* **2021**, *538*, 72–79. [CrossRef] [PubMed]
17. Choudhary, M.I.; Shaikh, M.; Tul-Wahab, A.; Ur-Rahman, A. In silico identification of potential inhibitors of key SARS-CoV-2 3CL hydrolase (Mpro) via molecular docking, MMGBSA predictive binding energy calculations, and molecular dynamics simulation. *PLoS ONE* **2020**, *15*, e0235030. [CrossRef] [PubMed]
18. Kabinger, F.; Stiller, C.; Schmitzova, J.; Dienemann, C.; Kokic, G.; Hillen, H.S.; Hobartner, C.; Cramer, P. Mechanism of molnupiravir-induced SARS-CoV-2 mutagenesis. *Nat. Struct. Mol. Biol.* **2021**, *28*, 740–746. [CrossRef] [PubMed]
19. Hammond, J.; Leister-Tebbe, H.; Gardner, A.; Abreu, P.; Bao, W.; Wisemandle, W.; Baniecki, M.; Hendrick, V.M.; Damle, B.; Simon-Campos, A.; et al. Oral Nirmatrelvir for High-Risk, Nonhospitalized Adults with COVID-19. *N. Engl. J. Med.* **2022**, *386*, 1397–1408. [CrossRef] [PubMed]
20. Yotsuyanagi, H.; Ohmagari, N.; Doi, Y.; Yamato, M.; Bac, N.H.; Cha, B.K.; Imamura, T.; Sonoyama, T.; Ichihashi, G.; Sanaki, T.; et al. Efficacy and Safety of 5-Day Oral Ensitrelvir for Patients with Mild to Moderate COVID-19: The SCORPIO-SR Randomized Clinical Trial. *JAMA Netw. Open* **2024**, *7*, e2354991. [CrossRef] [PubMed]
21. Zhou, Y.; Gammeltoft, K.A.; Ryberg, L.A.; Pham, L.V.; Tjornelund, H.D.; Binderup, A.; Hernandez, C.R.D.; Fernandez-Antunez, C.; Offersgaard, A.; Fahnoe, U.; et al. Nirmatrelvir-resistant SARS-CoV-2 variants with high fitness in an infectious cell culture system. *Sci. Adv.* **2022**, *8*, eadd7197. [CrossRef] [PubMed]
22. Doi, A.; Ota, M.; Saito, M.; Matsuyama, S. Sporadic Occurrence of Ensitrelvir-Resistant SARS-CoV-2, Japan. *Emerg. Infect. Dis.* **2024**, *30*, 1289–1291. [CrossRef] [PubMed]
23. Krismer, L.; Schoppe, H.; Rauch, S.; Bante, D.; Sprenger, B.; Naschberger, A.; Costacurta, F.; Furst, A.; Sauerwein, A.; Rupp, B.; et al. Study of key residues in MERS-CoV and SARS-CoV-2 main proteases for resistance against clinically applied inhibitors nirmatrelvir and ensitrelvir. *npj Viruses* **2024**, *2*, 23. [CrossRef] [PubMed]
24. Ip, J.D.; Chu, A.W.-H.; Chan, W.M.; Leung, R.C.-Y.; Abdullah, S.M.U.; Sun, Y.; To, K.K.-W. Global prevalence of SARS-CoV-2 3CL protease mutations associated with nirmatrelvir or ensitrelvir resistance. *eBioMedicine* **2023**, *91*, 104559. [CrossRef] [PubMed]
25. Esmaeili, S.; Owens, K.; Wagoner, J.; Polyak, S.J.; White, J.M.; Schiffer, J.T. A unifying model to explain frequent SARS-CoV-2 rebound after nirmatrelvir treatment and limited prophylactic efficacy. *Nat. Commun.* **2024**, *15*, 5478. [CrossRef] [PubMed]
26. Flores-Ocelotl, M.R.; Rosas-Murrieta, N.H.; Moreno, D.A.; Vallejo-Ruiz, V.; Reyes-Leyva, J.; Dominguez, F.; Santos-Lopez, G. Taraxacum officinale and Urtica dioica extracts inhibit dengue virus serotype 2 replication in vitro. *BMC Complement. Altern. Med.* **2018**, *18*, 95. [CrossRef] [PubMed]
27. Cruz-Arreola, O.; Orduna-Diaz, A.; Dominguez, F.; Reyes-Leyva, J.; Vallejo-Ruiz, V.; Dominguez-Ramirez, L.; Santos-Lopez, G. In silico testing of flavonoids as potential inhibitors of protease and helicase domains of dengue and Zika viruses. *PeerJ* **2022**, *10*, e13650. [CrossRef] [PubMed]
28. Kim, S.; Chen, J.; Cheng, T.; Gindulyte, A.; He, J.; He, S.; Li, Q.; Shoemaker, B.A.; Thiessen, P.A.; Yu, B.; et al. PubChem 2023 update. *Nucleic Acids Res.* **2023**, *51*, D1373–D1380. [CrossRef] [PubMed]
29. Pettersen, E.F.; Goddard, T.D.; Huang, C.C.; Couch, G.S.; Greenblatt, D.M.; Meng, E.C.; Ferrin, T.E. UCSF Chimera—A visualization system for exploratory research and analysis. *J. Comput. Chem.* **2004**, *25*, 1605–1612. [CrossRef] [PubMed]
30. Hanwell, M.D.; Curtis, D.E.; Lonie, D.C.; Vandermeersch, T.; Zurek, E.; Hutchison, G.R. Avogadro: An advanced semantic chemical editor, visualization, and analysis platform. *J. Cheminform.* **2012**, *4*, 17. [CrossRef] [PubMed]
31. Halgren, T.A. MMFF VI. MMFF94s option for energy minimization studies. *J. Comput. Chem.* **1999**, *20*, 720–729.
32. Berman, H.M.; Westbrook, J.; Feng, Z.; Gilliland, G.; Bhat, T.N.; Weissig, H.; Shindyalov, I.N.; Bourne, P.E. The Protein Data Bank. *Nucleic Acids Res.* **2000**, *28*, 235–242. [CrossRef] [PubMed]
33. Brunger, A.T. Free R value: A novel statistical quantity for assessing the accuracy of crystal structures. *Nature* **1992**, *355*, 472–475. [CrossRef] [PubMed]

34. Oerlemans, R.; Ruiz-Moreno, A.J.; Cong, Y.; Kumar, N.D.; Velasco-Velazquez, M.A.; Neochoritis, C.G.; Smith, J.; Reggiori, F.; Groves, M.R.; Domling, A. Repurposing the HCV NS3-4A protease drug boceprevir as COVID-19 therapeutics. *RSC Med. Chem.* **2020**, *12*, 370–379. [CrossRef] [PubMed]
35. Maier, J.A.; Martinez, C.; Kasavajhala, K.; Wickstrom, L.; Hauser, K.E.; Simmerling, C. ff14SB: Improving the Accuracy of Protein Side Chain and Backbone Parameters from ff99SB. *J. Chem. Theory Comput.* **2015**, *11*, 3696–3713. [CrossRef] [PubMed]
36. Trott, O.; Olson, A.J. AutoDock Vina: Improving the speed and accuracy of docking with a new scoring function, efficient optimization, and multithreading. *J. Comput. Chem.* **2010**, *31*, 455–461. [CrossRef] [PubMed]
37. Ravindranath, P.A.; Forli, S.; Goodsell, D.S.; Olson, A.J.; Sanner, M.F. AutoDockFR: Advances in Protein-Ligand Docking with Explicitly Specified Binding Site Flexibility. *PLoS Comput. Biol.* **2015**, *11*, e1004586. [CrossRef] [PubMed]
38. Besler, B.H.; Merz, K.M., Jr.; Kollman, P.A. Atomic charges derived from semiempirical methods. *J. Comput. Chem.* **1990**, *11*, 431–439. [CrossRef]
39. Domínguez-Ramírez, L.; Anaya-Ruiz, M.; Cortés-Hernández, P. Quality over quantity: How to get the best results when using docking for repurposing. *Front. Bioinform.* **2025**, *5*, 1536504. [CrossRef] [PubMed]
40. Liu, H.; Ye, F.; Sun, Q.; Liang, H.; Li, C.; Li, S.; Lu, R.; Huang, B.; Tan, W.; Lai, L. *Scutellaria baicalensis* extract and baicalein inhibit replication of SARS-CoV-2 and its 3C-like protease in vitro. *J. Enzym. Inhib. Med. Chem.* **2021**, *36*, 497–503. [CrossRef] [PubMed]
41. Case, D.A.; Aktulga, H.M.; Belfon, K.; Ben-Shalom, I.; Brozell, S.R.; Cerutti, D.S.; Cheatham, T.E., III; Cruzeiro, V.W.D.; Darden, T.A.; Duke, R.E. *Amber 2021*; University of California: San Francisco, CA, USA, 2021.
42. Llanos, M.A.; Gantner, M.E.; Rodriguez, S.; Alberca, L.N.; Bellera, C.L.; Talevi, A.; Gavernet, L. Strengths and Weaknesses of Docking Simulations in the SARS-CoV-2 Era: The Main Protease (Mpro) Case Study. *J. Chem. Inf. Model.* **2021**, *61*, 3758–3770. [CrossRef] [PubMed]
43. Zajaček, D.; Dunárová, A.; Bucinsky, L.; Štekláč, M. Compromise in Docking Power of Liganded Crystal Structures of Mpro SARS-CoV-2 Surpasses 90% Success Rate. *J. Chem. Inf. Model.* **2024**, *64*, 1628–1643. [CrossRef] [PubMed]
44. Onal, H.; Arslan, B.; Ergun, N.U.; Topuz, S.; Semerci, S.Y.; Kurnaz, M.E.; Molu, Y.M.; Bozkurt, M.A.; Suner, N.; Kocatas, A. Treatment of COVID-19 patients with quercetin: A prospective, single center, randomized, controlled trial. *Turk. J. Biol.* **2021**, *45*, 518–529. [CrossRef] [PubMed]
45. Di Pierro, F.; Khan, A.; Iqtadar, S.; Mumtaz, S.U.; Chaudhry, M.N.A.; Bertuccioli, A.; Derosa, G.; Maffioli, P.; Togni, S.; Riva, A.; et al. Quercetin as a possible complementary agent for early-stage COVID-19: Concluding results of a randomized clinical trial. *Front. Pharmacol.* **2022**, *13*, 1096853. [CrossRef] [PubMed]
46. Ziaei, S.; Alimohammadi-Kamalabadi, M.; Hasani, M.; Malekahmadi, M.; Persad, E.; Heshmati, J. The effect of quercetin supplementation on clinical outcomes in COVID-19 patients: A systematic review and meta-analysis. *Food Sci. Nutr.* **2023**, *11*, 7504–7514. [CrossRef] [PubMed]
47. Di Stadio, A.; D'Ascanio, L.; Vaira, L.A.; Cantone, E.; De Luca, P.; Cingolani, C.; Motta, G.; De Riu, G.; Vitelli, F.; Spriano, G.; et al. Ultramicronized Palmitoylethanolamide and Luteolin Supplement Combined with Olfactory Training to Treat Post-COVID-19 Olfactory Impairment: A Multi-Center Double-Blinded Randomized Placebo- Controlled Clinical Trial. *Curr. Neuropharmacol.* **2022**, *20*, 2001–2012. [CrossRef] [PubMed]
48. Roncati, L.; Marra, C.; Gravina, D.; Di Massa, G.; Della Rosa, N.; Adani, R. Ultramicronized Palmitoylethanolamide and Luteolin: Drug Candidates in Post-COVID-19 Critical Illness Neuropathy and Positioning-Related Peripheral Nerve Injury of the Upper Extremity. *J. Hand Microsurg.* **2024**, *16*, 100028. [CrossRef] [PubMed]
49. Di Petrillo, A.; Orru, G.; Fais, A.; Fantini, M.C. Quercetin and its derivates as antiviral potentials: A comprehensive review. *Phytother. Res.* **2022**, *36*, 266–278. [CrossRef] [PubMed]
50. Lu, P.; Zhang, T.; Ren, Y.; Rao, H.; Lei, J.; Zhao, G.; Wang, M.; Gong, D.; Cao, Z. A Literature Review on the Antiviral Mechanism of Luteolin. *Nat. Prod. Commun.* **2023**, *18*, 1934578X231171521. [CrossRef]
51. Ryu, Y.B.; Jeong, H.J.; Kim, J.H.; Kim, Y.M.; Park, J.Y.; Kim, D.; Nguyen, T.T.; Park, S.J.; Chang, J.S.; Park, K.H.; et al. Biflavonoids from *Torreya nucifera* displaying SARS-CoV 3CL(pro) inhibition. *Bioorg. Med. Chem.* **2010**, *18*, 7940–7947. [CrossRef] [PubMed]
52. Derosa, G.; Maffioli, P.; D'Angelo, A.; Di Pierro, F. A role for quercetin in coronavirus disease 2019 (COVID-19). *Phytother. Res.* **2021**, *35*, 1230–1236. [CrossRef] [PubMed]
53. Shadrack, D.M.; Deogratias, G.; Kiruri, L.W.; Onoka, I.; Vianney, J.M.; Swai, H.; Nyandoro, S.S. Luteolin: A blocker of SARS-CoV-2 cell entry based on relaxed complex scheme, molecular dynamics simulation, and metadynamics. *J. Mol. Model.* **2021**, *27*, 221. [CrossRef] [PubMed]
54. Munafo, F.; Donati, E.; Brindani, N.; Ottonello, G.; Armirotti, A.; De Vivo, M. Quercetin and luteolin are single-digit micromolar inhibitors of the SARS-CoV-2 RNA-dependent RNA polymerase. *Sci. Rep.* **2022**, *12*, 10571. [CrossRef] [PubMed]
55. Shahhamzehei, N.; Abdelfatah, S.; Efferth, T. In Silico and In Vitro Identification of Pan-Coronaviral Main Protease Inhibitors from a Large Natural Product Library. *Pharmaceuticals* **2022**, *15*, 308. [CrossRef] [PubMed]
56. Wei, F.; Gao, C.; Wang, Y. The role of influenza A virus-induced hypercytokinemia. *Crit. Rev. Microbiol.* **2022**, *48*, 240–256. [CrossRef] [PubMed]

57. Yong, Y.K.; Wong, W.F.; Vignesh, R.; Chattopadhyay, I.; Velu, V.; Tan, H.Y.; Zhang, Y.; Larsson, M.; Shankar, E.M. Dengue Infection—Recent Advances in Disease Pathogenesis in the Era of COVID-19. *Front. Immunol.* **2022**, *13*, 889196. [CrossRef] [PubMed]
58. Montazersaheb, S.; Khatibi, S.M.H.; Hejazi, M.S.; Tarhriz, V.; Farjami, A.; Sorbeni, F.G.; Farahzadi, R.; Ghasemnejad, T. COVID-19 infection: An overview on cytokine storm and related interventions. *Virol. J.* **2022**, *19*, 92. [CrossRef] [PubMed]
59. Jasso-Miranda, C.; Herrera-Camacho, I.; Flores-Mendoza, L.K.; Dominguez, F.; Vallejo-Ruiz, V.; Sanchez-Burgos, G.G.; Pando-Robles, V.; Santos-Lopez, G.; Reyes-Leyva, J. Antiviral and immunomodulatory effects of polyphenols on macrophages infected with dengue virus serotypes 2 and 3 enhanced or not with antibodies. *Infect. Drug Resist.* **2019**, *12*, 1833–1852. [CrossRef] [PubMed]
60. Al-Khayri, J.M.; Sahana, G.R.; Nagella, P.; Joseph, B.V.; Alessa, F.M.; Al-Mssallem, M.Q. Flavonoids as Potential Anti-Inflammatory Molecules: A Review. *Molecules* **2022**, *27*, 2901. [CrossRef] [PubMed]
61. Yao, J.; Zhang, Y.; Wang, X.Z.; Zhao, J.; Yang, Z.J.; Lin, Y.P.; Sun, L.; Lu, Q.Y.; Fan, G.J. Flavonoids for Treating Viral Acute Respiratory Tract Infections: A Systematic Review and Meta-Analysis of 30 Randomized Controlled Trials. *Front. Public Health* **2022**, *10*, 814669. [CrossRef] [PubMed]